FRIPONMeter : high resolution radiometer for fireballs

M. Lebreton[1], H. Constans[1], F. Colas[2], P. Vernazza[5], A. Malgoyre[5], S. Bouley[8,4], B. Zanda[9,4], S. E. Anderson[6,4], P. Shober[7,4], J. L. Rault[2,4], D. Darson[1], S. Anghel[2,3], D. Baratoux[10], M. Birlan[2,3], S. Bouquillon[2], J. Gattacceca[11], S. Jeanne[2], L. Jorda[5], A. Lagain[11], L. Maquet[2], J. Vaubaillon[2] and P.M. Zanetta[12]

[1] Lab. de Physique de l'Ecole Normale Supérieure, ENS, Univ. PSL, CNRS, Sorbonne Univ., France [2] LTE, Observatoire de Paris, Université PSL, Sorbonne Université, LNE, CNRS, Paris, France [3] Astronomical Institute of the Romanian Academy, Bucharest, Romania [4] FRIPON (Fireball Recovery and InterPlanetary Observation) and Vigie-Ciel Team, France [5] Laboratoire d'Astrophysique de Marseille - Pythéas - Marseille - France [6] Université Côte d'Azur, OCA, CNRS, Laboratoire Lagrange, Nice, France [7] NASA Astromaterials Research and Exploration Science Division, Johnson Space Center, Houston, USA [8] Université Paris-Saclay, UMR CNRS 8148, GEOPS, Orsay, France [9] Institut de Minéralogie, Muséum National d'Histoire Naturelle, CNRS, Paris, 75005, France [10] Géosciences Environnement Toulouse, Université de Toulouse, CNRS IRD, Toulouse, France [11] CEREGE, CNRS, AMU, IRD, PYTHEAS, Aix-en-Provence, France [12] LGL-TPE UMR5276 (CNRS, UCBL1, ENS Lyon, UJM), Saint-Étienne, France

The FRIPON network has been operating for ten years, enabling the recovery of two meteorites in France and contributing to the recovery of five others across Europe. The fall of 2023 CX1 demonstrated that precise knowledge of the altitude of catastrophic fragmentation is essential for computing the dark flight and, consequently, the strewn field. This altitude can be determined through accurate measurements of surges in the light curve. Although this is possible using camera data, the acquisition rate (30 fps) is often too low, and saturation issues arise for very bright events such as meteorite-producing fireballs. Light curves also provide insights into the mechanical strength of meteoroid material and can help determine whether it has a brittle composition similar to that of cometary material. The European Fireball Network was the first to install radiometers alongside fisheye cameras. This article presents a prototype designed for the FRIPON network that can also operate as a standalone instrument. Its main features include precise timing, a high acquisition rate (2 kHz), and an extended dynamic range, enabling observations from small fireballs detectable by FRIPON to extremely bright events capable of producing meteorites.

1 Fireball light curves

Light curves of atmospheric entries provide access to several physical parameters of the incoming object. One of the most important is the initial mass, which can be estimated from the measurement of the total radiated light energy of the phenomenon. This quantity can be converted into kinetic energy using the luminous efficiency coefficient. The main difficulty with this method, which has been addressed by many authors (Drolshagen et al., 2021b; Johnston et al., 2024; Loehle et al., 2024; Subasinghe et al., 2018), is the estimation of the luminous efficiency coefficient. This parameter depends on several factors, such as the initial velocity, entry angle, and composition of the meteoroid. According to these studies, the luminous efficiency can vary by up to two orders of magnitude. A dedicated study based on FRIPON data (Drolshagen et al., 2021a) used masses derived from atmospheric deceleration measurements at high altitude (Jeanne et al., 2019).

Light curves can also be used to identify fragmentation events, which manifest as sudden bursts of brightness. These features provide information about the mechanical strength of the material, as the dynamic pressure responsible for fragmentation can be estimated from the altitude and the speed of these events. The precise timing of brightness bursts allows the fragmentation altitude to be determined using the kinematic model derived from the triangulation of camera observations. For this analysis, light curves must therefore be accurately time-stamped and have sufficient temporal resolution.

1.1 Previous developments

Attempts to measure meteor light curves using long exposures date back to the first networks employing photographic plates in the Czech Republic (Ceplecha, 1961). which used rotating shutters, and extend to more recent systems such as the Desert Fireball Network (DFN) in Australia, which uses digital cameras equipped with liquid-crystal shutters (Bland et al., 2012; Devillepoix et al., 2018). In 2010, the All-Sky Video Meteor Network in Southern Ontario, Canada — the ASGARD system (Brown et al., 2010) — was established. Using analog video cameras, it enabled the recovery of the Grimsby meteorite (Brown et al., 2011). Later, networks such as FRIPON (Colas et al., 2020) adopted digital cameras. However, the light curves obtained by all these networks share common limitations, particularly

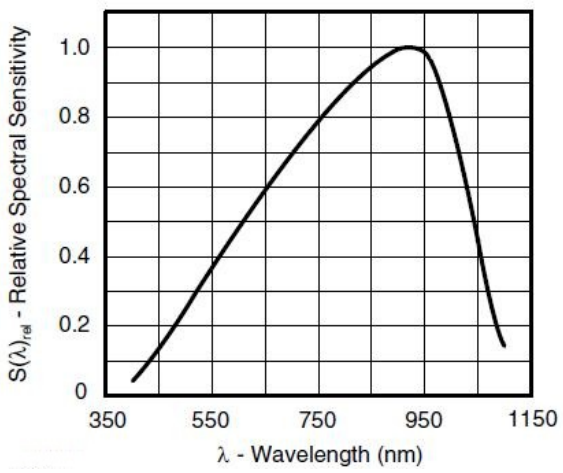

Figure 1 – Photodiode spectral sensitivity.

in terms of acquisition speed and image saturation for bright events.

For this reason, the European Fireball Network was the first to install radiometers alongside fisheye cameras (Spurný et al., 2002). These radiometers were initially based on photomultipliers operating at 500 Hz and later at 5 kHz. Subsequently, radiometers based on photodiodes were developed (Buchan et al., 2019; Popowicz et al., 2025; Rault, 2020; Vida et al., 2015), but none have been deployed on a scale comparable to that of the European Fireball Network.

1.2 Radiometer versus camera

It is important to combine these two types of receivers because cameras allow photometric calibration using background stars, which radiometers do not. However, radiometers have a much higher temporal resolution and do not saturate during very bright events. By combining the two approaches, it is possible to obtain a light curve that can be used to measure the total luminous flux and, subsequently, the initial kinetic energy via the luminous efficiency coefficient. Finally, from the kinematic model obtained by triangulating observations from several stations, a photometry-based estimate of the initial mass can be derived. For non-saturated large bolides, this provides one of the best estimations of the pre-entry mass (Anghel et al., 2021). The DFN tested the use of high-speed digital cameras (470 fps) and showed that they can be used as stand-alone instruments for both trajectory determination and unsaturated light-curve measurements (Giancono et al., 2026). Radiometer measurements, however, cover the entire sky and can have an even higher sampling rate and sensitivity. They are therefore more affected by variations in sky brightness (diffuse sky background, Moon, aircraft, light pollution, etc.). Although it can produce false detections, they are generally easier to filter out. Anghel et al. (2023) showed that machine-learning techniques can filter more than 98% of false positives in FRIPON-MOROI data, surpassing human performance.

1.3 Specification aims

Since the photometer is intended for fireball detection networks, and more specifically for FRIPON, the detection threshold must be close to magnitude −3. For the brightest observable event, we based our calculations on the Chelyabinsk fireball (Brown et al., 2013), which had an absolute magnitude of −28, close to that of the Sun (−27). However, for such bright events, it is not necessary to obtain unsaturated data from stations located close to the fall; more distant cameras can easily be used. Therefore, this criterion on the brightest event observable without saturation is not mandatory. Based on previous experiments, in particular those conducted by the Czech team (Spurný et al., 2002), an acquisition rate of a few kHz appears sufficient both to limit saturation and to study fragmentations, which require a minimum temporal resolution on the order of a millisecond.

2 Design presentation

2.1 Photodiode measurement principle

The radiometer performs wide dynamic range measurements using a set of low-cost photodiodes. The Vishay Silicon PIN photodiode is specified with a 5 $\mu A/W/m^2$ sensitivity at 950 nm, and its estimated sensitivity to solar spectral irradiance is 3.5 $\mu A/W/m^2$. The spectral bandwidth sensitivity is that of a PIN silicon diode, with a maximum in the near infrared. The half-sensitivity range spans from 600 nm to 1050 nm (Figure 1).

The BPW34 photodiode is suitable for both low- and high-level measurements owing to different bias schemes (Figure 2):

- Low-level measurements are performed by parallelizing 65 photodiodes operating at zero bias voltage.
- High-level measurements are performed by a single photodiode using up to 10 V bias voltage.

In addition, the design of the amplifiers and ADC converters requires careful attention to optimize the signal-to-noise ratio. The sensitive area of a single photodiode is 7.5 mm^2, while the total area of the complete matrix of 67 photodiodes is 500 mm^2. The photodiodes are mounted on a 41×41 mm horizontal flat surface, protected by a glass screen, and occluded at 45° by the aluminum housing window (Figure 3).

The sensitivity of the photodiodes decreases to 50% at 25° elevation; this value is adopted for the complete radiometer, according to the average position of the 65 diodes behind the metal housing window. The single diode covering the upper range is located at the center of the matrix. Furthermore, the photodiode matrix is shielded from electrical noise by a grounded grid, which also slightly attenuates incoming light; this attenuation is negligible in the absence of an optical front device.

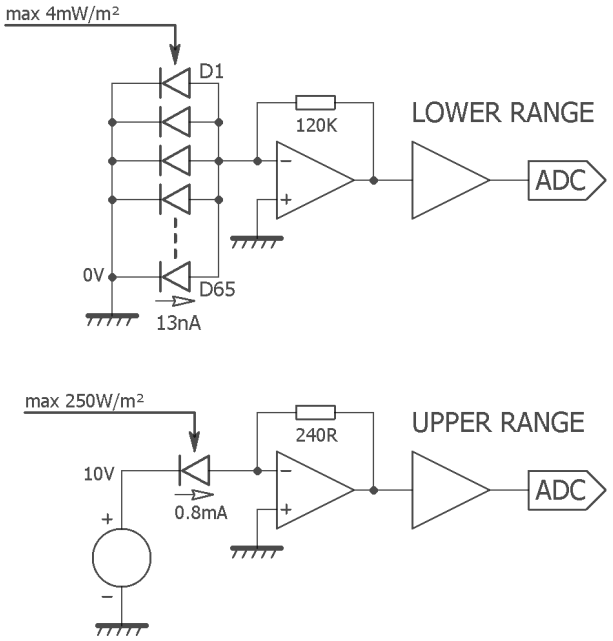

Figure 2 – Photodiode amplifier schematic.

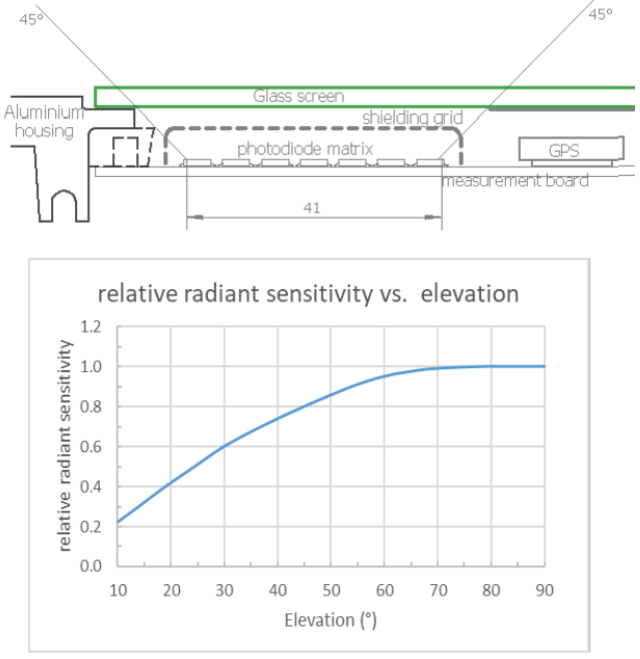

Figure 3 – Photodiode matrix window profile.

2.2 Measurement range

Maintaining both amplitude resolution and signal-to-noise ratio throughout the entire dynamic range is achieved by three simultaneous acquisition channels: high range = 250 W/m^2, medium range = 1 W/m^2, and lower range = 4 mW/m^2. The photometer continuously records 16-bit raw data from three simultaneous analog-to-digital converters. Post-processing of the data is necessary to select the appropriate range or to combine multiple ranges when the dynamic range exceeds that of a single channel. Since the gains and offsets of the three channels vary with temperature and aging, the processing is performed independently for each event.

Post-processing of the data is also necessary to remove

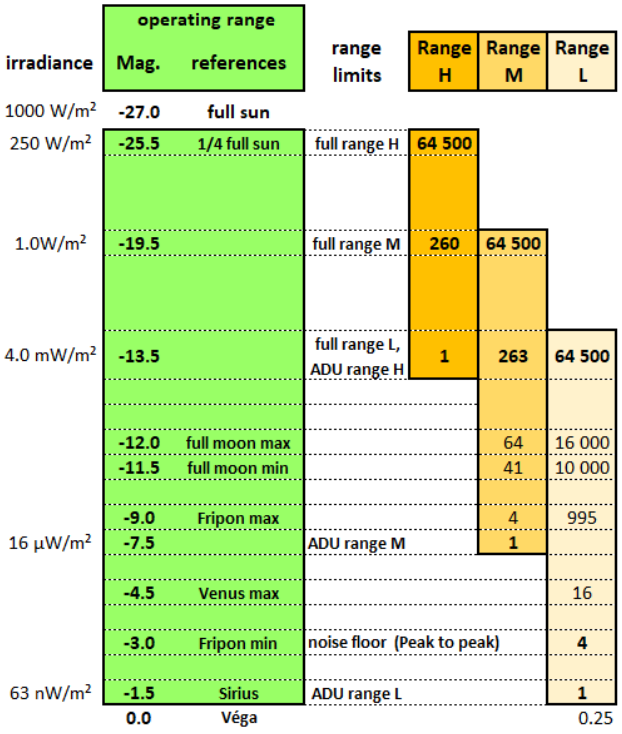

Figure 4 – Operating range.

the continuous sky background in order to calculate the instrumental magnitude of each event. Finally, these data are adjusted to those provided by the cameras to obtain a light curve calibrated in absolute magnitude. The operating range table (Figure 4) summarizes the key performance characteristics of this design.

The main performance features are as follows:

- The low range is sufficiently sensitive and broad to monitor faint events, even when the full moon increases the sky background light.
- The high range, with a maximum level up to 25% of full sunlight, is sufficient to fully capture any large event.
- The noise-free dynamic range reaches 1.0×10^9, corresponding to a 30-bit noise-free resolution.
- The specified noise amplitude is peak-to-peak over the full bandwidth of 0.8 kHz. Additional post-processing filtering allows the user to increase the effective resolution up to 4.0×10^9 (32 bits), based on the rms noise level.

The maximum observable magnitude is therefore −25.5, which does not reach the target of −27. However, as explained in Section 1.3, this is sufficient for an extended network. This saturation limit can be compared with those of different networks: DFN at magnitude −15 (Neidhart et al., 2021), FRIPON at magnitude −9 (Colas et al., 2020), SonataCO at magnitude −6, and GMN at magnitude 0 (Vida et al., 2021). Apart from DFN and FRIPON, the latter networks are primarily dedicated to meteor observations rather

than to fireballs. Nevertheless, as demonstrated by the 2023 CX1 fall (Egal et al., 2025), combining data from multiple networks is always beneficial, and the use of FRIPONMeter during the 2023 CX1 event would have been of great help by providing high-time-resolution radiometric measurements, thus improving light curve reconstruction, fragmentation sequence and energy estimates.

2.3 Hardware and connection design

The radiometer comprises six internal functional blocks (Figure 5):

1. 67-photodiode matrix;
2. 3-range measurement circuit;
3. temperature sensor;
4. GPS/GNSS receiver for accurate time stamping;
5. digital circuitry with microcontroller and Ethernet controller;
6. isolated DC/DC converter and voltage regulators.

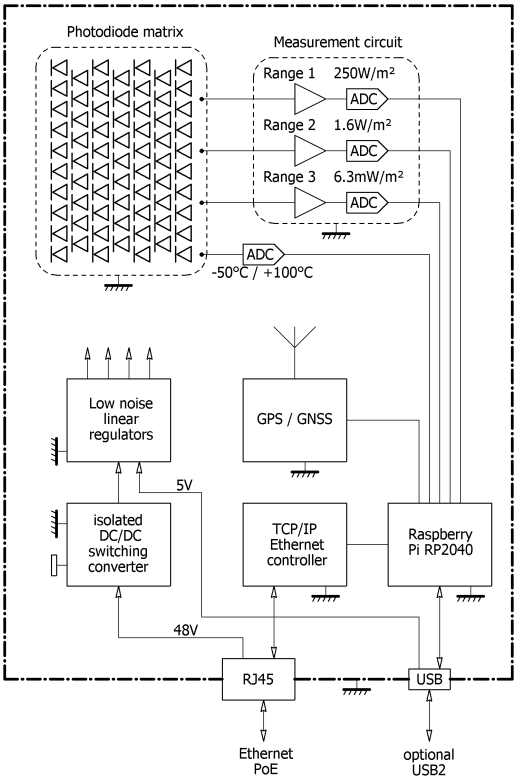

Figure 5 – Hardware description.

The radiometer can be operated using one of two available external connections:

- The optimal performance is achieved via the Ethernet PoE (RJ45) connection, which provides both network access and an isolated power supply. In this mode, the radiometer is integrated into the existing FRIPON camera system network (Fig. 6).
- Alternatively, a USB connection is available for simple standalone operation with a nearby PC.

Whatever the external connection scheme, the low-level measurement requirements critically influence the hardware design. The lowest irradiance resolution, 63 $\mathrm{nW/m^2}$ (magnitude −1.5), corresponds to a photodiode current of only 0.2 pA. To enable accurate measurement of such a low-level current, several optimizations have been implemented:

- The 65-photodiode matrix increases the amplifier input current to 13 pA. However, the capacitive input noise also increases proportionally with the total surface area of the matrix.
- The input stage employs a high-quality, low-noise amplifier and low-value gain resistors.
- Internal digital filtering suppresses high-frequency switching noise from the power supply.
- All circuitry is shielded using common ground planes.
- The photodiode matrix itself is shielded with a grounded metallic front grid.
- The radiometer shielding ground must be connected to the mains earth via an FTP-shielded RJ45 cable and a compatible PoE switch.

This final optimization is mandatory to ensure the radiometer's performance. Conventional PoE switches with 48 V DC power supplies are designed for applications where electrical noise coupling is relevant only in terms of EMC standards and operator safety. Accordingly, the metal housing and shielding are not connected to the mains earth. Furthermore, the internal transformer isolation of low-cost 48 V DC power supplies is poor: stray capacitances can drive significant 50 Hz AC currents to the connected devices (i.e., common-mode currents). If unmitigated, these currents can leak through the RJ45 cable, the photodiode matrix, and its capacitive surface to earth; during a darkness test, a 50 Hz input noise of 400 ADU was measured in the lower range. To prevent this, an additional cable, connected as close as possible to the PoE switch outlet, grounds the metal housing and shielding of the PoE switch, as illustrated in Figure 5. When using the optional non-isolated USB connection for standalone operation with a local PC, it is important to ensure that the PC is itself properly grounded to the mains earth.

2.4 Mechanical design

The radiometer prototype was designed and tested using a waterproof plastic enclosure with a 150 × 85 × 80 mm polycarbonate transparent lid, as illustrated in Figure 7. The next version will use a waterproof aluminum 159 × 86 × 60 mm enclosure fitted with a glass screen integrated into the lid, as shown in Figure 8.

Table 1 – Measurement system specifications (ambient temperature = 25°C, unless otherwise specified).

Parameter	Test condition	Value
ADC converter resolution	either range	16 bits
Differential linearity	either range	± 0.6 ADU (i.e., LSB)
High range resolution	Sun light spectral irradiance at sea level	3.87E-03 W/m^2/ADU
Medium range resolution	Sun light spectral irradiance at sea level	1.56E-05 W/m^2/ADU
Low range resolution	Sun light spectral irradiance at sea level	6.34E-08 W/m^2/ADU
Dark current + Bias current offset	Darkness, any range	530 ADU
Offset thermal drift	−25°C / +50°C	2 ADU/°C
H. range / M. range gain ratio	nominal value	249
M. range / L. range gain ratio	nominal value	245
Gain thermal drift	−25°C / +50°C	0.1%/°C
Peak-to-peak noise high range	darkness & optical shutter 100 ms acquisition	1 ADU
Peak-to-peak noise medium range	darkness & optical shutter 100 ms acquisition	2 ADU
Peak-to-peak noise low range	darkness & optical shutter 100 ms acquisition	4 ADU
Internal filter cutoff frequency	−3 dB	0.8 kHz
Settling time at 99%	Light step test	1 ms
Data recording rate		2 kHz

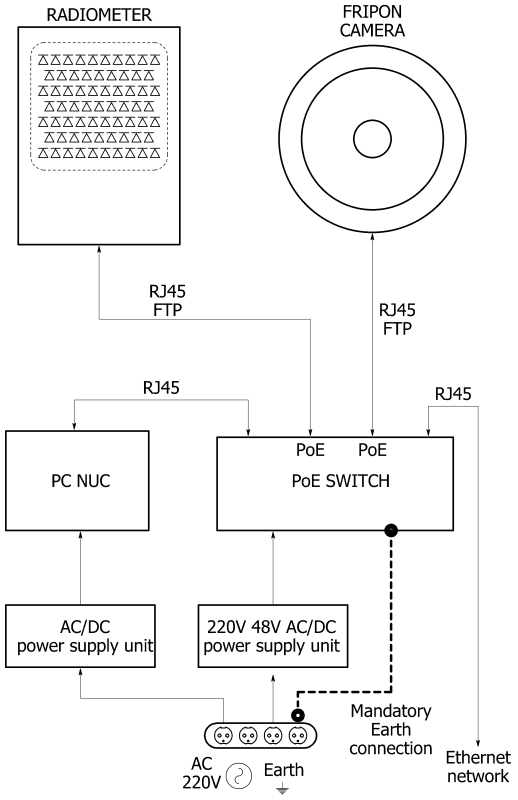

Figure 6 – Ethernet PoE FRIPON network.

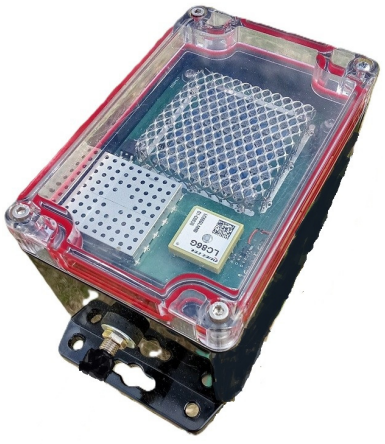

Figure 7 – Radiometer prototype A.

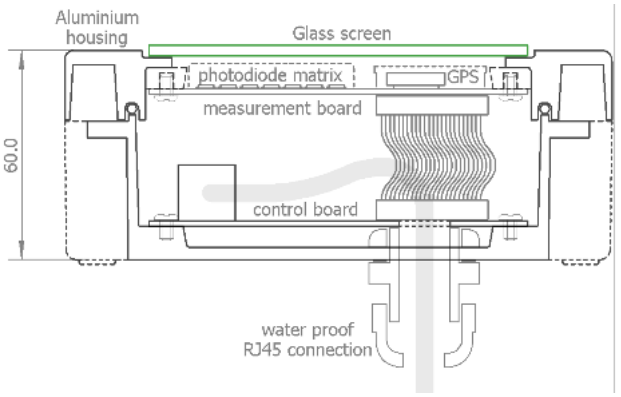

Figure 8 – Radiometer version B.

2.5 Software and data storage

The photometer onboard computer is based on a Raspberry Pi Pico RP2040 microcontroller. Its embedded firmware initializes a TCP server, performs ADC readings every 20 µs, and applies a first-order infinite impulse response (IIR) low-pass filter to these samples. The radiometer digital specifications are shown in Table 2. One second of data is stored in a 2k-sample buffer, corresponding to a 500 µs sampling interval. When a remote computer is connected, the acquisition buffer is transmitted every second. Measurement values are sent as raw hexadecimal numbers from the 16-bit unsigned ADC output. Each buffer is labeled with a GPS timestamp, the photometer temperature, and a sample count. Data are lost if no remote computer is connected. A TCP client on the same network can continuously read the data frames. Table 3 summarizes the storage specifications without size optimization.

Table 2 – Radiometer digital specifications

Time	Memory size
Internal sampling frequency	50 kHz for each range
Internal digital filter	IIR first order low-pass
Quantization	2 kHz
Recording time stamping resolution	± 500 µs
Data frame size jitter	± 1 sample
Max. internal clock frequency drift	50 ppm/°C

Table 3 – Data storage specifications.

Time	Data	Content	Memory size
1 s	frame	2k samples × 3 ranges	24 kB
1 min	file	60 frames	1.4 MB
1 day	directory	1440 files	2.1 GB
1.3 year	disk drive	480 days	1 TB

3 Tests on the sky

3.1 2025 Perseid meteor shower

We took advantage of the 2025 Perseid meteor shower to organize an observation campaign at the Pic du Midi observatory, even though this year was not favorable due to a very bright moon. With detection statistics being low for the FRIPON network (two or three detections per week per station), it was important to take advantage of one of the largest meteor showers of the year. We chose the Pic du Midi observatory (Figure 9) because it is equipped with a FRIPON camera that allows photometric calibration of events .

Figure 9 – FRIPON camera and radiometer at Pic du Midi.

3.2 One event data processing example

Data frames from the radiometer are continuously recorded by the remote PC, which also controls the FRIPON camera. Each frame contains the raw acquisition data from the three simultaneous ranges over a one-second interval.

- When FRIPON detects a fireball near the Pic du Midi, the corresponding data frame is retrieved for further analysis.
- The electronic offset and sky background are estimated by averaging the signal over a 10-second interval before and after the event. A light curve in arbitrary units (ADU) is then extracted and calibrated using the FRIPON pipeline to derive absolute magnitudes.
- A low-pass digital filter may be applied in post-processing to enhance the signal-to-noise ratio for faint events with slow temporal variations.

As an example, a fireball was recorded on 2025-08-12 at 01:53:29 UT from Pic du Midi (Figure 10). The background sky brightness was 8275 ADU, corresponding to nearly full-moon conditions (magnitude −11.3). This demonstrates that even under full-moon conditions, the radiometer is capable of recording fast and faint events at its maximum temporal resolution. The detection threshold is magnitude −2.5, in agreement with the instrument specifications.

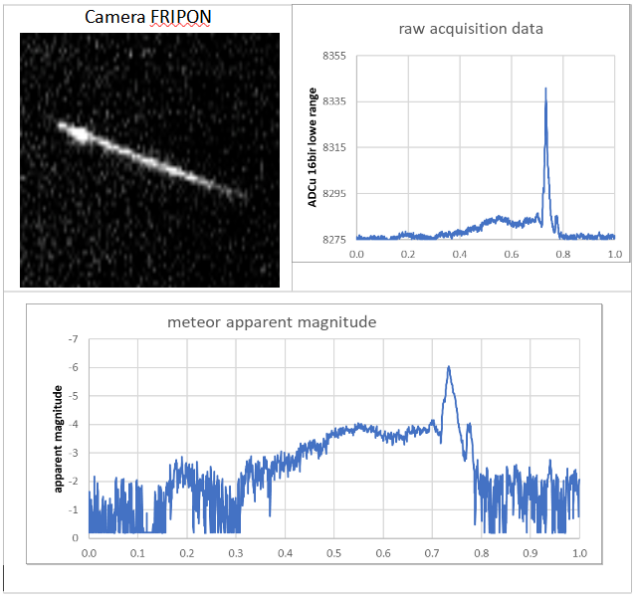

Figure 10 – Fireball detected on 2025-08-12 at 01:53:29 UT observed from Pic du Midi. Top right: raw linear data, bottom: absolute magnitude data calibrated with FRIPON camera data.

3.3 Calibration on sky

The gain of the lower dynamic range is computed by comparing data from the FRIPON camera and the radiometer (Fig. 11), both located at the same site. A single unsaturated bright event is used for this calibration: peak magnitude −8, elevation 64°, altitude 96 km, and distance 105 km.

The processing steps are as follows:

1. Data centered around the event are retrieved.
2. A digital post-processing filter with a cutoff frequency of 80 Hz and a settling time of 10 ms is applied to reduce the readout noise.
3. A constant level of 2545 ADU, corresponding to both the electronic offset and the sky background (approximately magnitude −10), is subtracted.
4. The radiometer gain is manually fitted to obtain the best alignment between the camera and radiometer light curves.

The radiometer apparent magnitude of the event is computed using Equation 1:

$$mag = -2.5 \times \log\left(\frac{ADU}{gain}\right) \quad (1)$$

The difference between the factory gain value of 0.275 (computed using the estimated photodiode sensitivity to solar spectral irradiance of 3.5 $\mu A/W/m^2$) and the gain calibrated on the sky, 0.25, is less than 9%.

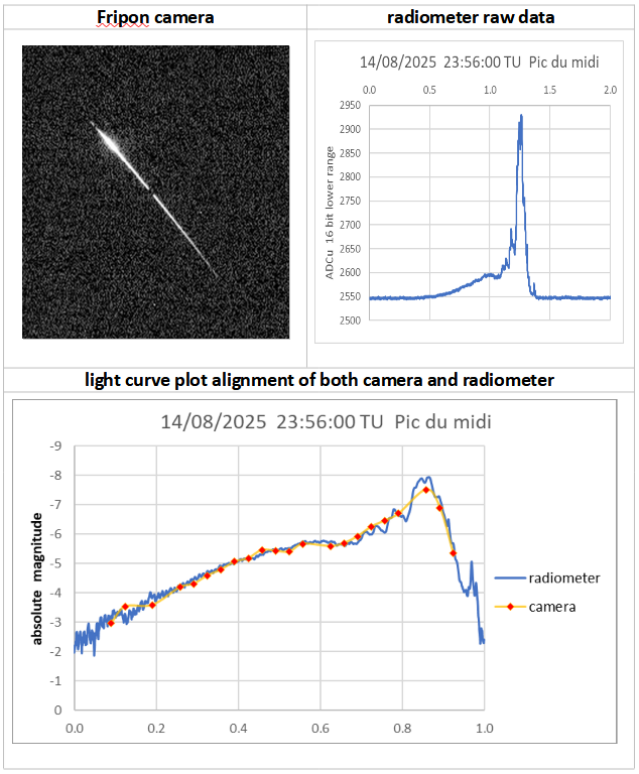

Figure 11 – Photometric calibration.

Since no comparison between the camera and the radiometer is available at high signal levels, the gains of the medium and high ranges are calibrated relative to the low range gain. Twilight sky brightness is used to obtain several measurement points across the transitions between low and medium ranges, and then between medium and high ranges. These transitions provide a sufficiently wide overlap to allow a linear interpolation over several points and thus determine an accurate gain ratio. The difference between the gain ratios (high/medium or medium/low) derived from the factory specifications (at 25°C) and those measured on the sky is less than 1.5%.

3.4 Interference events

The main source of light pollution is public lighting, which is modulated at 100 Hz (twice the grid frequency). This issue motivates the installation of both the camera and the radiometer at sites that are as high and remote as possible. Several other types of events can bias the fireball monitoring; fortunately, they mainly produce short, high-speed spikes that are easy to distinguish from a meteor light curve. Moreover, these short events provide a convenient way to test the response time of the radiometer over a wide range of amplitudes. An example recording of a thunderstorm lightning flash during daylight, obtained using the high range (maximum 250 W m^{-2}), is shown in Fig. 12. Because the light pulse is shorter than the sampling period, the recorded pulse shape corresponds to the response of the internal 800 Hz low-pass filter (only three samples × 0.5 ms = 1.5 ms).

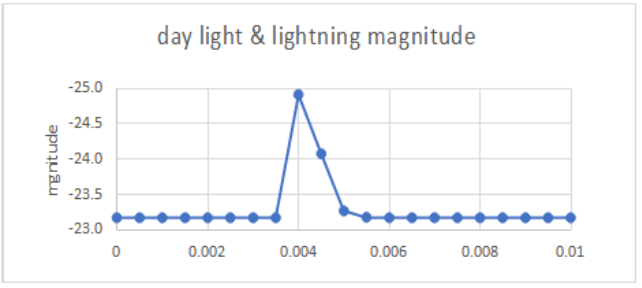

Figure 12 – Thunderstorm lightning recorded during daylight.

An example of a nearby airliner with periodically flashing lights is shown in Fig. 13. The duration of each light pulse is shorter than the radiometer sampling period of 0.5 ms. Consequently, the periodic pattern exhibits varying amplitudes. The burst record lasts for several minutes, corresponding to the time required for the aircraft to cross the sky. A small meteor event occurs simultaneously, demonstrating that this type of interference can be easily removed from the final data.

4 Next steps and conclusions

As the technical characteristics of this radiometer prototype comply with the specifications, its overall design (photodiodes, analog-to-digital converters, and PoE power supply) will be retained for the development and manufacture of a new prototype. However, several modifications will be introduced. In particular, a USB control interface will be added, allowing more flexible use in networks that do not employ the FRIPON configuration (Colas et al., 2020), which relies on a PoE connection.

In addition, PoE control components will be integrated into the digital board, resulting in a simplified architecture with only two electronic boards: one dedicated to the photodiodes with analog-to-digital conversion and GPS, and a second handling power supply and communication with the control PC. Finally, a new metal enclosure with a glass window will be used in order to maximize the operational lifetime of the radiometer.

During the *Pic du Midi* observational run, events occurring at distances greater than 200 km were detected. Because the FRIPON network is very dense (median inter-station distance ∼80 km), radiometeres are not required at every station. One instrument every 160 km is sufficient. We therefore plan to manufacture approximately 100 units to equip 25 stations in France, 50 worldwide, and keep 25 as spare units. The manufacturing plans will be released as open-source hardware so that they can be freely replicated. We plan to manufacture and test this second prototype in 2026 and to begin mass production in 2027.

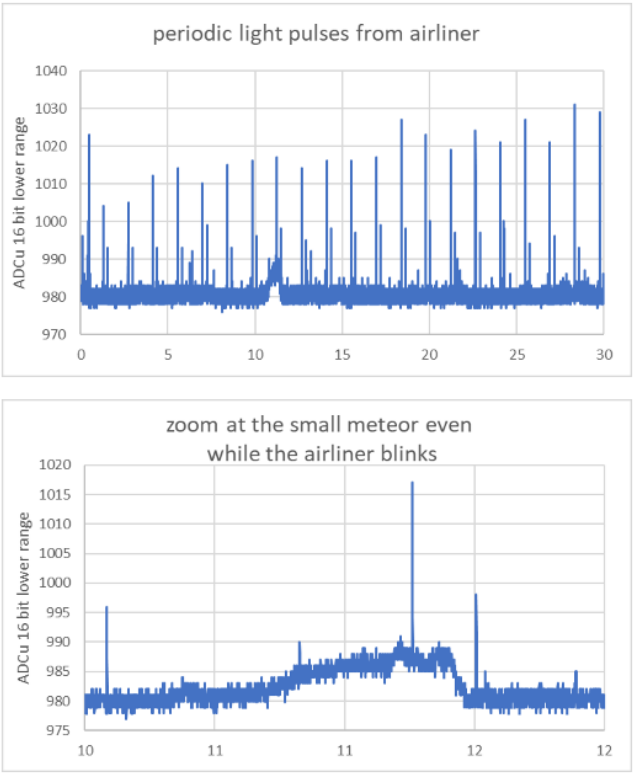

Figure 13 – Periodic light pulses from a nearby airliner.

References

Anghel S. et al. (2021). "Energy signature of ton TNT-class impacts: analysis of the 2018 December 22 fireball over Western Pyrenees". *MNRAS*, **508:4**.

Anghel S., Nedelcu D. A., Birlan M., and Boaca I. (2023). "Single-station meteor detection filtering using machine learning on MOROI data". , **518**.

Bland P. et al. (2012). "The Australian Desert Fireball Network: a new era for planetary science". *Australian Journal of Earth Sciences*, **59:2**, 177–187.

Brown P. et al. (2010). "Development of an All-Sky Video Meteor Network in Southern Ontario, Canada The ASGARD System". *WGN*, **38:1**, 25–30.

Brown P. et al. (2011). "The fall of the Grimsby meteorite—I: Fireball dynamics and orbit from radar, video, and infrasound records". *MPS*.

Brown P. G. et al. (2013). "A 500-kiloton airburst over Chelyabinsk and an enhanced hazard from small impactors". *Nature*, **503:7475**, 238–241.

Buchan S. et al. (2019). "Developing a Cost-Effective Radiometer for Fireball Light Curves". In *IMC2019*.

Ceplecha Z. (1961). "Multiple fall of Přibram meteorites photographed". *Bulletin of the Astronomical Institutes of Czechoslovakia*, **12**, 21.

Colas F. et al. (2020). "FRIPON: a worldwide network to track incoming meteoroids". *A & A*, **644**, A53.

Devillepoix H. A. R. et al. (2018). "Observation of metre-scale impactors by the desert fireball network". *MNRAS*, **483:4**, 5166–5178.

Drolshagen E., Ott T., et al. (2021a). "Luminous efficiency based on FRIPON meteors and limitations of ablation models". *A & A*, **650**, A159.

Drolshagen E., Ott T., et al. (2021b). "Luminous efficiency of meteors derived from ablation model after assessment of its range of validity". *A / A*, **652**, A84.

Egal A. et al. (2025). "Catastrophic disruption of asteroid 2023 CX1 and implications for planetary defence". *Nature Astronomy*.

Giancono D. et al. (2026). "Photometry of Fireballs using High Frame Rate Cameras". *arXiv e-prints*.

Jeanne S. et al. (2019). "Calibration of fish-eye lens and error estimation on fireball trajectories: application to the FRIPON network". *A & A*, **627**, A78.

Johnston C. et al. (2024). "Assessment of meteoroid preatmospheric diameter from brightness measurements prior to fragmentation". *Icarus*, **408**, 115807.

Loehle S. et al. (2024). "Meteorite material luminous efficiencies from ground testing of meteoroid entry". *Icarus*, **407**, 115817.

Neidhart T. et al. (2021). "Statistical analysis of fireballs: Seismic signature survey". *Publications of the Astron. Soc. of Australia*, **38**, e016.

Popowicz A. et al. (2025). "Enhancing meteor observations with photodiode detectors". *Applied Sciences*.

Rault J.-L. (2020). "A little tour across the wonderful realm of meteor radiometry". In *IMC2020*.

Spurný P. et al. (2002). "The autonomous all-sky photographic camera for meteor observation". In Warmbein B., editor, *ACM 2002*.

Subasinghe D. et al. (2018). "Luminous Efficiency Estimates of Meteors. II. Application to Canadian Automated Meteor Observatory Meteor Events". *Astronomical Journal*, **155:2**, 88.

Vida D. et al. (2015). "Low-cost meteor radiometer". In Rault J. L. and Roggemans P., editors, *IMC2015*.

Vida D. et al. (2021). "The Global Meteor Network - Methodology and first results". *MNRAS*, **506**.